Aerodynamic and Acoustic Interactions Associated with Inboard Propeller-Wing Configurations

Nikolas S. Zawodny,* D. Douglas Boyd Jr., † and Douglas M. Nark ‡

NASA Langley Research Center, Hampton, VA, 23681

A series of aerodynamic performance and acoustic measurements have been made on a range of inboard propeller-wing interaction configurations in the NASA Langley Low Speed Aeroacoustic Wind Tunnel (LSAWT). The results presented in this paper are part of a more expansive testing campaign encompassing both single propeller-wing and multipropeller-wing interactions, the former of which is discussed in the present work. The primary testing parameters of interest to this study are the axial and vertical positioning of the wing relative to the propeller slipstream under a constant propeller advance ratio. A multifaceted computational effort was also employed in an effort to identify reflection and scattering effects imposed by both the wing geometry as well as the primary components of the facility test setup. This effort consisted of aerodynamic predictions using high-fidelity computational fluid dynamics (CFD), acoustic predictions using an impermeable Ffowcs Williams and Hawkings (FW-H) solver, and acoustic scattering predictions. Acoustic measurements reveal variations in the acoustic directivity behavior of the propeller blade passage frequency for even modest variations in wing position. CFD-based acoustic predictions reveal discrepancies relative to the experimental data, which is believed to be due to complex acoustic scattering behavior within the test section. Initial attempts at modeling the scattered acoustic field showed functional dependency of the acoustic amplitude variations on the wing position relative to the propeller disk; however, discrepancies with experimental data remain.

Nomenclature

c	Wing chord, m
c_s	Transducer sleeve chord, m
c_∞	Ambient speed of sound, m/s
C_p	Steady pressure coefficient, $(P_s - P_\infty) / \frac{1}{2}\rho_\infty U_\infty^2$
C_Q	Propeller torque coefficient, $Q/\rho_\infty n^2 D_p^5$
C_T	Propeller thrust coefficient, $T/\rho_\infty n^2 D_p^4$
D_p	Propeller diameter, m
J	Propeller advance ratio, U_∞/nD_p $(= \pi M_\infty / M_{\text{tip}})$
M_∞	Tunnel freestream Mach number, U_∞/c_∞
n	Propeller rotation rate, revolutions per second
Q	Propeller torque, N*m
R	Propeller radius, m
T	Propeller thrust, N
U_∞	Tunnel freestream velocity, m/s
α_P	Propeller geometric angle of attack, deg.
α_W	Wing geometric angle of attack, deg.
ΔX	Axial distance of wing leading edge from propeller tip (rel. R)
ΔZ	Vertical distance of wing leading edge from propeller axis of rotation (rel. R)
θ	Observer flyover angle, deg.
ρ_∞	Ambient air density, kg/m^3

*Research Aerospace Engineer, Aeroacoustics Branch, Member AIAA; nikolas.s.zawodny@nasa.gov

†Senior Research Engineer, Aeroacoustics Branch; d.d.boyd@nasa.gov

‡Senior Research Engineer, Structural Acoustics Branch, AIAA Associate Fellow; douglas.m.nark@nasa.gov

ψ Observer azimuthal angle, deg.
Ω Propeller rotation rate, RPM

I. Introduction

Recent years have shown an unprecedented emergence of numerous vehicle concepts for urban air mobility (UAM) operations. Due to the large variety of vehicle types, there has, consequently, been an emergence of a large number of either new or more prevalent aeroacoustic sources. A summary of some of these noise sources is presented in Fig. 1. Figure 1(a) shows the expected aeroacoustic noise sources associated with a tiltwing vehicle concept in both vertical takeoff and landing (VTOL) and cruise phases of flight. It is worth noting that the sources highlighted in green represent those that have been frequently investigated in the past, are better understood, and are more easily modeled.[1,2] Furthermore, Fig. 1(b) provides an illustration of the expected interactional noise sources associated with an inboard distribution of propellers along the leading edge of an aircraft wing. These sources are expected to include (however, are not necessarily limited to) the following:

- Scattering and/or shielding of propeller acoustic source(s) resulting in a change in source directivity.
- Effects of the wing potential field on propeller blade loading, resulting in a modification of the incident propeller noise source.
- Impingement of the propeller wake on the wing surface, affecting the aerodynamic performance of the system and producing additional wing loading noise.

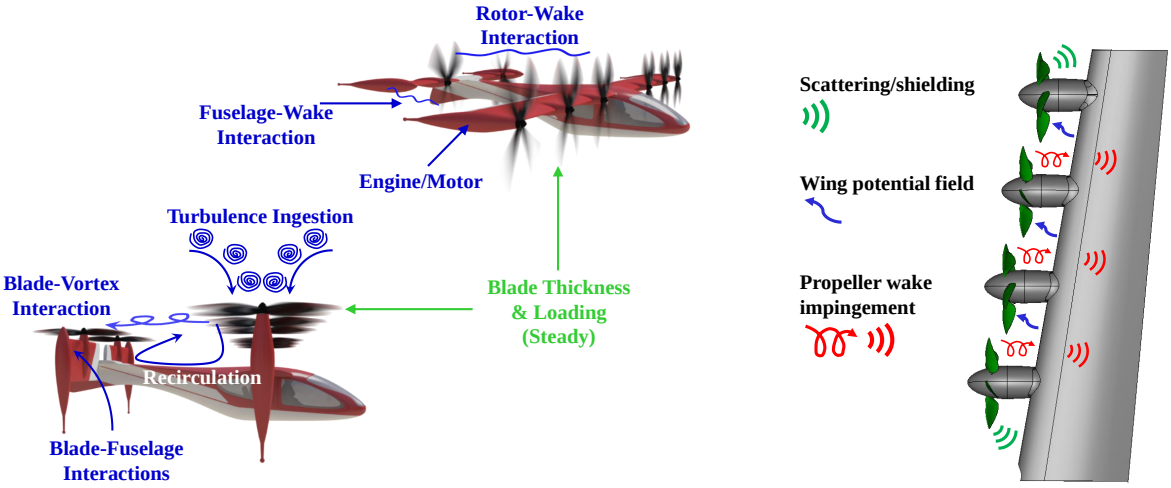

(a) Tiltwing Noise Sources (b) Propeller-Wing Noise Sources

Figure 1. Noise sources associated with UAM vehicle concepts.

This paper aims to identify the presence and relative roles of the noise source mechanisms representative of a UAM vehicle concept implementing an inboard, wing leading edge-mounted propeller or array of propellers.

II. Technical Approach

This study encompasses a combined experimental and computational investigation; the former incorporating performance and acoustic testing in an aeroacoustic wind tunnel, and the latter incorporating computational fluid dynamics (CFD) and time-domain acoustic scattering predictions.

A. Experimental Setup

1. *The LSAWT*

The LSAWT is an open-circuit free jet wind tunnel that is currently configured for a freestream Mach number range of $0.045 \leq M_\infty \leq 0.140$; however, it has an upper end capability of $M_{\infty,\max} = 0.32$. The test chamber is acoustically treated with an approximate cut-off frequency of 250 Hz, and is outfitted with a 28-element linear array of 6.35 mm-diameter B&K model 4939 free-field microphones. The linear array microphone in closest proximity to the propeller tested in this study ($\theta = 90°$) is at a radial distance of 3.5 m (138") from the propeller hub. The test section length (from inlet trailing edge to flow collector leading edge) is approximately 5.6 m, and the circular inlet nozzle diameter is $D_{\text{nozzle}} = 1.93$ m. Respective mean flow and turbulent velocity surveys of the test section at $M_\infty = 0.10$ have identified a core flow size of radius $r_C \approx 0.42 D_{\text{nozzle}}$ and a centerline turbulence intensity of $TI = 0.054\%$ at an axial location of $x/D_{\text{nozzle}} = 0.855$ downstream of the inlet nozzle trailing edge.[3] The propeller tested in this study is positioned at an approximate downstream location of $x/D_{\text{nozzle}} = 0.645$ for all tests.

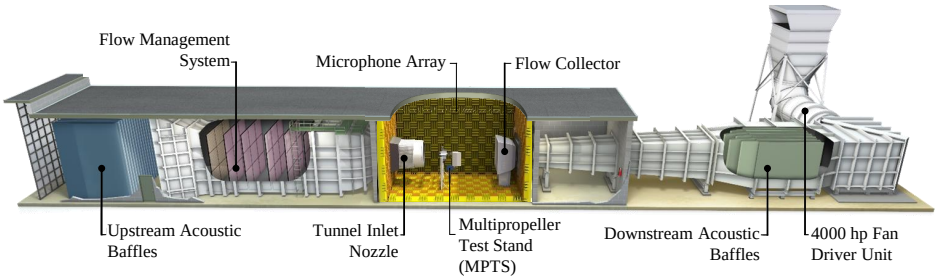

Figure 2. Rendered cutaway illustration of the LSAWT.

2. *Multipropeller Test Stand and Traversable Wing Assembly*

The LSAWT multipropeller test stand (MPTS) is capable of mounting an array of up to three propellers simultaneously in a linear arrangement, normal to the tunnel freestream flow. Only two propellers were tested simultaneously in this testing campaign due to a combination of the size of the propellers tested in this study and the LSAWT open-jet test section core flow restrictions.[3] An image of the MPTS with two propellers installed is provided in Fig. 3(a). It is important to note that the results documented in this paper are those for a single propeller-wing interaction configuration, which is detailed more in Section II.A.4. As this image shows, propellers are positioned upstream of a model fairing using a flat mounting plate

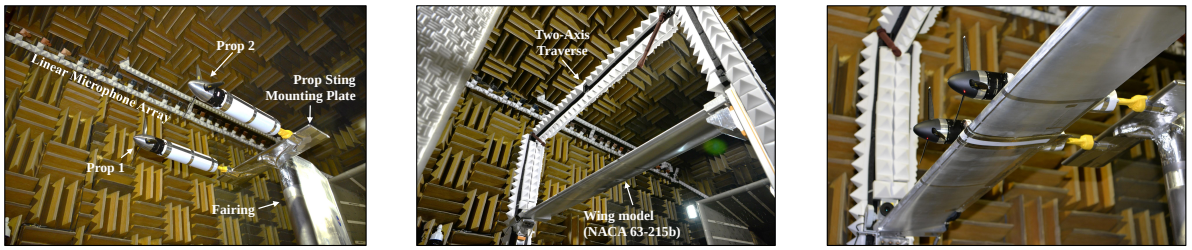

(a) Multipropeller Test Stand (b) Traversable Wing Assembly (c) Propeller-Wing Setup

Figure 3. Primary components of the propeller-wing testing apparatus in the LSAWT test section. Note: flow is from left to right, wing installed "upside down".

from which the propeller stings are extruded. The propeller stings are covered by hollow plastic cylindrical nacelle fairings. The propellers and motors are powered using the same power/control system detailed in Reference 4.

The propeller tested in this study is a Mejzlik 16x11, 3-bladed carbon fiber propeller, which has a tip radius of $R = 0.2$ m (7.875"). The wing tested is a 0.914-m (36") wide, 0.406-m (16") chord NACA $63_2 - 215$ MOD B airfoil,[5] previously utilized for studies of wake/flap interaction noise.[6] The effective width of the airfoil was increased to approximately 2.44 m (96") with the use of fabricated airfoil profile extension pieces. The resulting wing model thus protrudes approximately 0.254 m (10") through each side of the LSAWT

open-jet shear layer. The wing is supported by a two-axis traverse system, shown in Fig. 3(b). The traverse system consists of two tall vertical supports and a top horizontal reinforcement beam, all of which were positioned outside of the test section flow. The wing was traversed vertically and axially relative to the stationary MPTS. An image of the complete multipropeller-wing test setup is provided in Fig. 3(c). It is important to note that the wing is installed inverted in the test section such that the linear microphone array views the wing lower surface.

3. Aerodynamic Measurement Capabilities

Propeller and wing aerodynamics were assessed using a combination of a multiaxis load cell for propeller loads, and wing steady and unsteady pressure surveys. Figure 4 provides a transparent view of the propeller sting assembly, with focus on the propeller load cell. As Fig. 4 shows, the load cell used in this study is

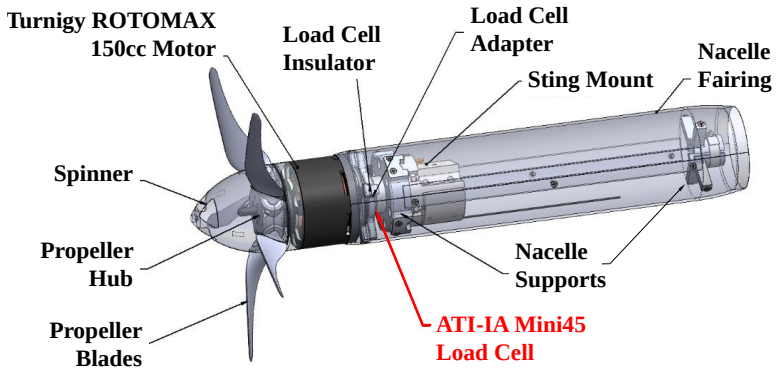

Figure 4. Transparent view of the propeller sting assembly. Note: Propeller shown is not the one tested in the current study.

an ATI-IA Mini45 load cell positioned just aft of the propeller motor. Due to considerable heating of the motor during propeller operations, a plastic insulator serves as a buffer between motor and load cell to help mitigate thermal drift of the load cell. It should be noted that a small air gap between the motor base and nacelle fairing was maintained so that the load cell measurement face was not physically bridged.

Figure 5(a) provides details of the steady and unsteady pressure measurement locations on the wing. Steady pressures were measured using two chordwise rows of built-in pressure taps. These rows are spaced 203 mm (8") apart and are centered about the propeller centerline. This provides a measurement of the propeller slipstream approximately corresponding to a propeller blade midspan location on both advancing and retreating sides of the propeller. Unsteady pressures were measured using a rapid-prototyped "sleeve" populated with a distribution of 16 Kulite LQ-064 sensors. The sleeve was fabricated to match the contour of the airfoil and has a thickness of 3.2 mm (0.125"). The design of this sleeve is partially based on a similar one tested on a pylon immersed in the slipstream of a tip-mounted propeller configuration in Reference 7. Half of the sensors were allocated for the suction side and the rest on the pressure side of the wing. The sleeve was positioned at two spanwise locations on the wing for this test: centered on the propeller axis of rotation, and at a lateral distance of 0.866R from the axis of rotation on the advancing side of the propeller. These two survey locations were chosen in order to measure the unsteady pressures on the wing associated with the inboard wake of the passing propeller blade and with the propeller tip vortex impingement, respectively. More specifically, the lateral offset location of 0.866R is intended to measure tip vortex impingement phenomena for wing positions of $\Delta Z/R = 0.5$. Figure 5(b) provides a rendering of the kulite sleeve detailing the instrumentation and wiring configurations. Note that the blue and red shaded portions of this image represent the two different fabricated pieces of the sensor sleeve that are adhered to each other upon installation on the wing model. Sensor positions were emulated from those tested in the propeller-pylon experiments conducted in Reference 7, which are reproduced in Fig. 5(c). It is important to note that the suction side sensor located at $0.90c_s$ was not functional at the onset of testing. Therefore, only the first seven suction-side transducers were available for this study.

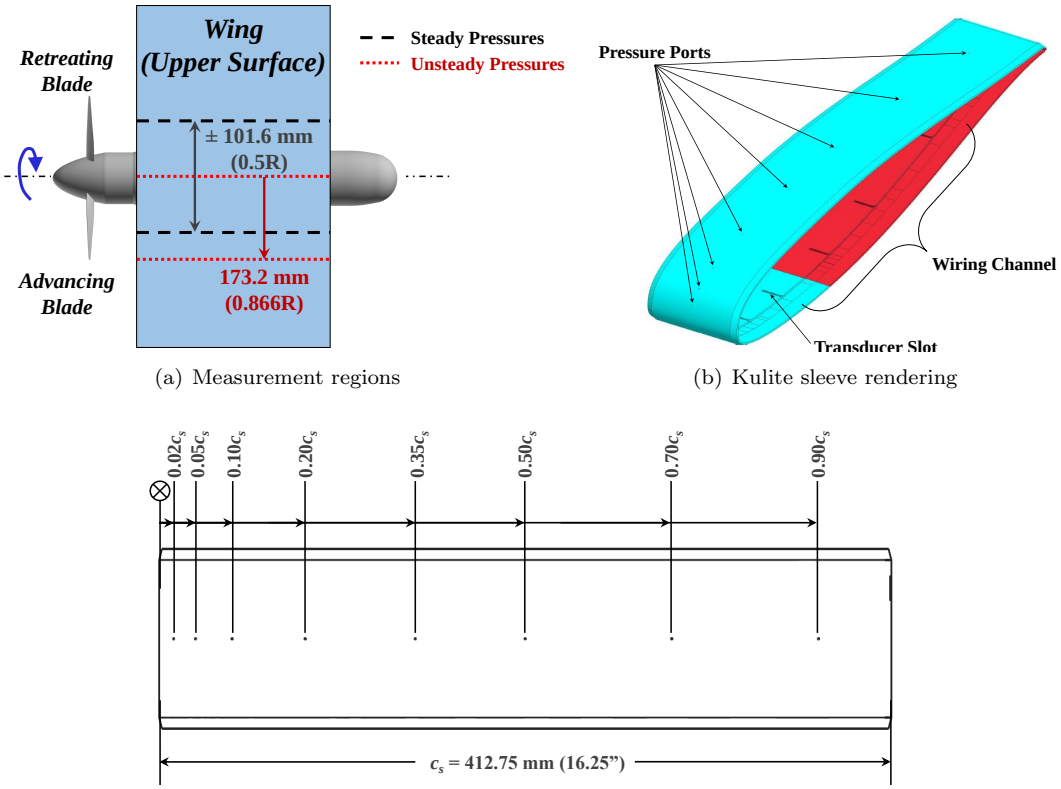

(a) Measurement regions

(b) Kulite sleeve rendering

(c) Kulite sensor locations

Figure 5. Illustrations of wing steady and unsteady pressure measurement regions, with unsteady pressure measurement sleeve details.

4. Testing Conditions

A schematic of the propeller-wing setup with pertinent dimensional parameters is provided in Fig 6(a). As mentioned previously, the current study focuses on single propeller-wing interaction configurations. This was achieved by replacing the second propeller with a blank spinner that remained stationary (nonrotating) during testing (see Fig. 6(b)). While a range of propeller advance ratios were tested, the majority of the propeller-wing interaction tests were performed at $J \approx 0.592$. The primary testing parameters are provided in Table 1. The wing is traversed to a grid of leading edge coordinates defined by the bounds indicated in Table 1 and visually portrayed in Fig. 6(c).

Table 1. Propeller-wing testing parameters.

	Parameter	Value
Propeller	Advance Ratio, J	0.592
	M_{tip}	0.361
	M_∞	0.068
	$\alpha_P, (^\circ)$	0, +5
Wing	$\Delta X/R$	0.25 $\Rightarrow$ 2.0
	$\Delta Z/R$	0.50 $\Rightarrow$ 1.5
	$\alpha_W, (^\circ)$	0, +5

5. Data Acquisition and Processing

Dynamic data were acquired on a National Instruments$^{\text{TM}}$ PXIe-1085 hybrid chassis populated with a combination of PXIe-4480 and PXI-6143 dynamic signal acquisition modules. Microphone data were acquired on the PXIe-4480 modules at a sampling rate of 102.4 kHz, while load cell and unsteady surface pressure probe data were acquired on the PXI-6143 modules at a slightly lower sampling rate of 80 kHz. This reduction in sampling rate was done in order to allow real-time monitoring of the propeller performance data. Time indices of the propeller revolution were recorded on both sets of modules using a Monarch ROLS-p laser sensor and ACT-3X tachometer system. Bandpass filtering of the microphone data provided a usable flat passband of less than -0.1 dB deviation within a frequency range of 50Hz $\leq f \leq$ 40 kHz. Load cell and surface pressure probe data were DC-coupled and low-pass filtered at a frequency of 40 kHz. Dynamic data

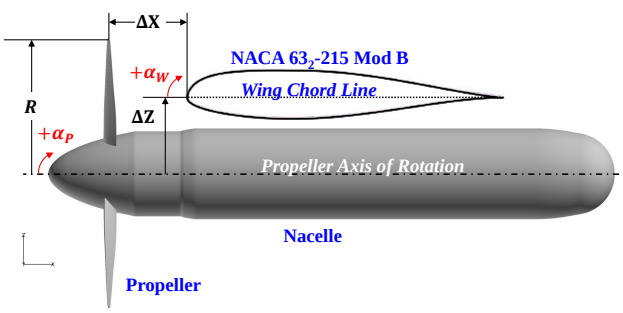

(a) Propeller-Wing Schematic

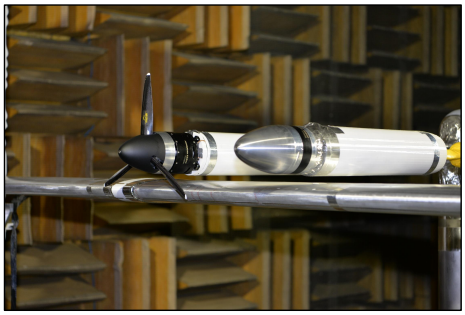

(b) Single Propeller-Wing Test Setup

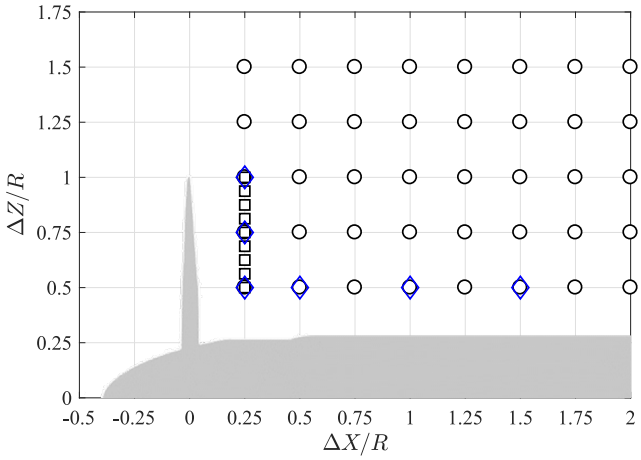

(c) Measurement Grid

Figure 6. Single propeller-wing schematic, LSAWT test setup, and grid representation of tested and simulated wing leading edge locations. Image (c): '◯' represent the coarse wing leading edge locations, '□' represent vertical fine sweep leading edge locations, and '◇' represent OF2 simulation wing leading edge locations. Note that images (a) and (c) are inverted relative to the LSAWT test setup depicted in (b).

for each test run condition were acquired for a time duration of 12 seconds.

Periodic averaging of dynamic data was performed on a per-revolution basis of the propeller system in order to provide a robust means of comparison with prediction data. The laser sensor/tachometer system mentioned above was used to parse dynamic data into individual propeller revolutions, with which an average revolution of data could be computed. While this method provides a means for analyzing both periodic and residual (broadband) components of noise, only periodic noise is pertinent to the current investigation. More details on this signal processing technique can be found in References 4 and 8.

B. Prediction Methodologies

Two acoustic prediction methods are considered in this study: a high-fidelity method incorporating aerodynamic loading from a CFD solution into a Ffowcs Williams and Hawking (FW-H) solver, and a time-domain acoustic scattering method. The former of these methods is intended to solve for the acoustic field representative of the hydrodynamic interactions associated with the propeller-wing condition, while the latter is intended to help identify additional noise sources such as reflections and scattering in the testing facility.

1. OVERFLOW2/PSU-WOPWOP (OF2-PSW)

CFD simulations were performed on the isolated propeller and propeller-wing cases using OVERFLOW2,[9] (herein referred to as OF2) which is an unsteady Reynolds-averaged Navier-Stokes (URANS) code. The simulation is explicit in nature, in which multiple propeller revolutions are simulated until convergence is

obtained. The optimized second-order backward differencing formulation BDF2OPT was utilized with a variable number of Newton subiterations per physical time step such that the L_∞-norm(RHS) achieved two orders of convergence at each subiteration. Each case was run for a total of 15 revolutions: the first ten revolutions were run at a coarse time resolution corresponding to 2.5° azimuthal increments, and the latter five at 0.25° azimuthal increments. The computational grid was constructed using overset grid generation via the Chimera Grid Tools v2.1 software package.[10] The OF2 simulations performed for this study were set to match the propeller operating condition detailed in Table 1 at sea-level standard day conditions, the wing positions depicted in Fig. 6(c), and a geometric wing angle of attack of $\alpha_W = 0°$. This produced a total of six propeller-wing simulation cases, and one isolated propeller simulation case. It is worth noting that the simulated wing geometry is a truncated representation of the one tested in LSAWT, spanning a total width of 1.2 m (47.25"). Computational surface definitions of the propeller blades and wing were generated from high resolution surface scans of the respective tested components. Figure 7 provides a sample OF2 visualization of the flow field solution at a single time step.

Acoustic predictions are performed using the CFD-provided impermeable loading data on the propeller, spinner, nacelle, and wing surfaces. These data are used as inputs to the FW-H solver, PSU-WOPWOP,[2] to compute acoustic pressure time histories at defined observer locations. One rotor revolution of CFD data is computed at a physical time resolution corresponding to 0.25° azimuthal increments, and are then downsampled to 1° azimuthal increments before being used as inputs to the acoustic solver and run as a periodic case. The process in which the impermeable surface pressure loadings from OF2 are used to compute an acoustic prediction using PSU-WOPWOP is herein denoted as OF2-PSW.

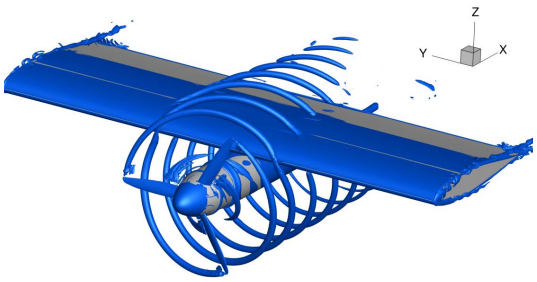

Figure 7. Isosurfaces of Q-criterion for propeller-wing OVERFLOW2 simulation case at a single time step; $\left(\frac{\Delta X}{R}, \frac{\Delta Z}{R}\right) = (0.50, 0.50)$.

2. *TD-FAST*

The final acoustic prediction tool considered in this study is the Time Domain Fast Acoustic Scattering Toolkit (TD-FAST).[11] As the name implies, this solver computes a scattered acoustic field in the time domain, containing all frequencies of the solution in a single computation. The purpose of these predictions is to help assess the potential impacts of both the wing and surrounding facility hardware on the radiated tonal acoustics. Figure 8 depicts the TD-FAST computational domain. The surfaces used in the current scattering predictions are depicted in Fig. 8(b); however, the capability exists for future iterations to incorporate all surfaces shown in Fig. 8(a). Scattering predictions are performed using a simple point (monopole) source positioned at the propeller hub location; however, the capability exists for future investigations to use more complex incident source fields, including the OF2-PSW prediction. All scattering surfaces are modeled as sound hard (fully reflective).

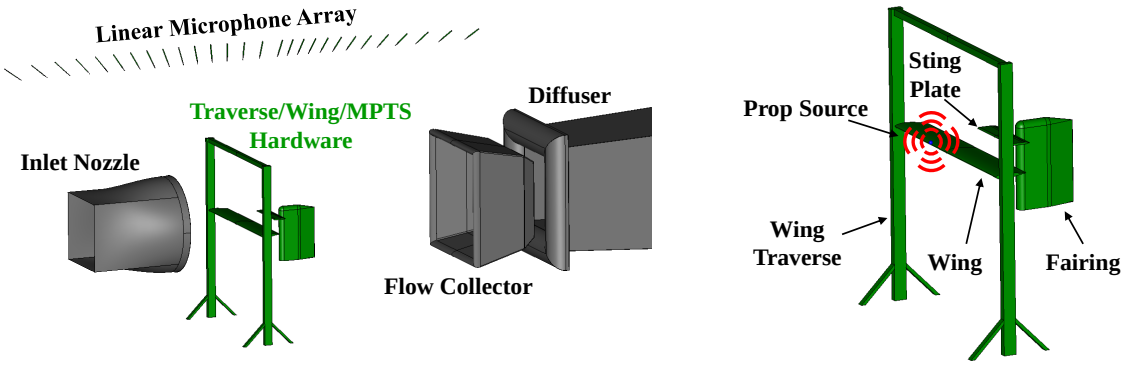

(a) TD-FAST computational domain

(b) Close-up view of scattering surfaces

Figure 8. Images and definitions of TD-FAST computational domain. Note: surfaces used in current scattering predictions are colored green.

III. Results

This section presents aerodynamic and acoustic results of the isolated propeller and propeller-wing configurations. Aerodynamic measurements in the form of propeller loads, wing steady pressure profiles, and wing unsteady pressures are presented, followed by acoustic measurements. Each section is accompanied by computational counterparts for the appropriate propeller-wing conditions.

A. Aerodynamic Measurements

1. *Propeller Loads*

An initial assessment of the ability of OF2 to model the propeller performance was done by comparing the predicted aerodynamic loads with the experimentally measured values. These results are summarized in Table 2. As these results show, the OF2 predictions considerably underpredict the LSAWT measurements. It was later found, however, that increasing the propeller collective angle by +1 degree in the simulation reduced the differences in C_T and C_Q to +0.5% and -2.2%, respectively. Unfortunately, this change to the simulation case setup could not be incorporated to the propeller-wing simulations due to time restrictions. As a result of these discrepancies, the following thrust trends for the propeller-wing configurations are presented in the form of percentage differences from the isolated propeller thrust coefficient.

Table 2. Isolated propeller load comparisons.

Force Coeff.	LSAWT	OF2	% Diff.
C_T	0.0874	0.0796	-8.9
C_Q	0.0128	0.0111	-13.3

Figure 9 shows the variation of the measured propeller thrust coefficient, C_T, with wing position for the three different pairs of propeller and wing angles of attack. All three conditions show an increase in

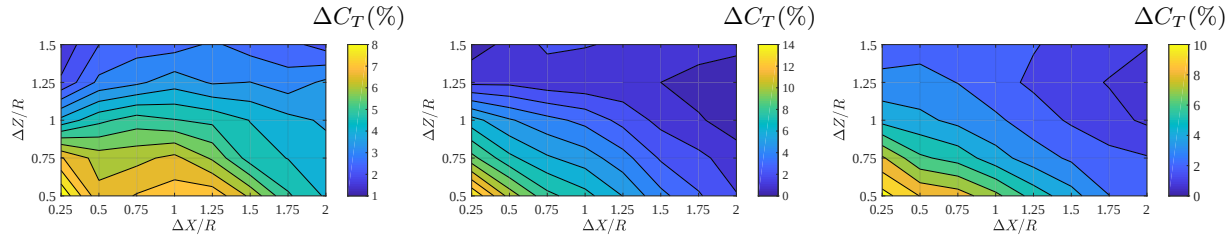

(a) $(\alpha_P, \alpha_W) = (0°, 0°)$ (b) $(\alpha_P, \alpha_W) = (0°, +5°)$ (c) $(\alpha_P, \alpha_W) = (+5°, +5°)$

Figure 9. Variation of propeller thrust coefficient with wing position for three different sets of propeller and wing angle of attack combinations. Data presented in percentage differences relative to isolated propeller values.

propeller-generated thrust for close wing proximities in both axial and vertical directions, with a reduction to the approximate isolated propeller thrust condition for the furthest wing positions. The data reveal maximum increases in propeller thrust relative to the isolated condition of approximately 8%, 14%, and 10%, respectively. All of these measured maxima occur at the wing leading edge location of $\left(\frac{\Delta X}{R}, \frac{\Delta Z}{R}\right) = (0.25, 0.50)$. The middle condition of $(\alpha_P, \alpha_W) = (0°, +5°)$ shown in Fig. 9(b) is useful because it shows that the load cell is capable of measuring the differences associated with the relative potential field impact of the airfoil for different angles of attack. Even though the manufacturer-quoted uncertainties of this load cell are in excess of 5% of the isolated propeller C_T, hysteresis checks of the load cell during testing revealed repeatability errors to within 2% of the isolated propeller C_T.

Figure 10 compares the change in propeller thrust coefficient with wing position between OF2 predictions and LSAWT measurements. Figure 10(a) provides the LSAWT results from both the coarse grid measurement (emulated in Fig. 9(a)) as well as from the fine vertical sweep illustrated previously in Fig. 6(c). The two LSAWT data sets show reasonable agreement with one another; however, with some slight divergence at the two intermediate vertical wing positions, $\Delta Z/R = 0.75$ and 1.00. These are, however, within the approximated 2% hysteresis error bars that are also indicated in the figure. Furthermore, the OF2 predictions agree well with the LSAWT data trends, particularly with the fine sweep data set. The data comparisons of Fig. 10(b), however, show considerable deviations for axial wing positions $\Delta X/R > 0.5$. One possible explanation is the difference between the experimental setup and OF2 surface grid definition of the propeller motor/nacelle interface region, which is illustrated in Fig. 11. As this figure shows, the experimental motor/nacelle interface region consists of an exposed motor base with a flat plastic insulator plate, while the CFD mesh consists of a smooth surface transition. This difference is due to the experimental rig requiring

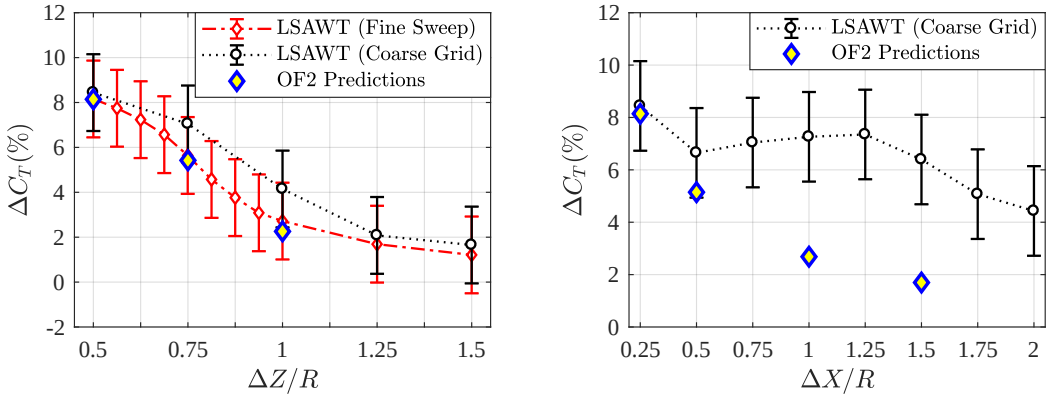

(a) Vertical wing positions ($\Delta X/R = 0.25$)

(b) Axial wing positions ($\Delta Z/R = 0.50$)

Figure 10. Comparison of propeller C_T variations with wing position between LSAWT measurements and OF2 predictions. All data shown are for $(\alpha_P, \alpha_W) = (0°, 0°)$.

modifications at the onset of testing to ensure both a thermally insulated and mechanically unbridged load cell configuration. Therefore, it is possible that the potential field of the wing at such a close proximity to the motor/nacelle region could augment the thrust generated by the propeller.

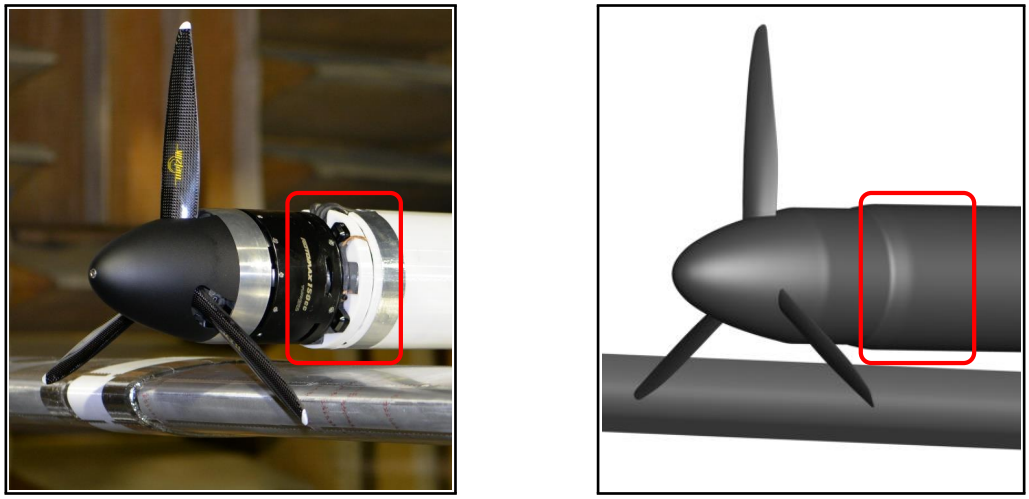

(a) Close-up of motor-nacelle region (LSAWT)

(b) Close-up of motor-nacelle region (OF2)

Figure 11. Illustrations of motor/nacelle interface region differences between experimental setup and OF2 simulation grid. Images represent a configuration of $\left(\frac{\Delta X}{R}, \frac{\Delta Z}{R}\right) = (0.25, 0.50)$.

To better visualize the impact of the wing on the loads generated by the propeller, Fig. 12 provides contours of axial Mach number, M_x, for all OF2 simulation cases at a plane located $0.15R$ ahead of the propeller. The wing potential field is clearly visible for the cases in the top row of this figure, represented by the considerable velocity deficit regions outside of the propeller disk and centered around the specified wing vertical location. Comparison of these cases to the isolated propeller case also reveals velocity deficits in the upper half of the propeller disk area, which are seen to decrease as the wing moves further vertically from the propeller centerline. The cases in the lower row of the figure are also seen to converge to the case of an isolated propeller as the wing is moved further downstream from the propeller disk.

2. Wing Steady Pressures

Figure 13 shows the wing pressure coefficient (C_p) distribution comparisons between LSAWT measurements and OF2 predictions for the three vertical wing positions simulated at $\Delta X/R = 0.25$. Note that the wing

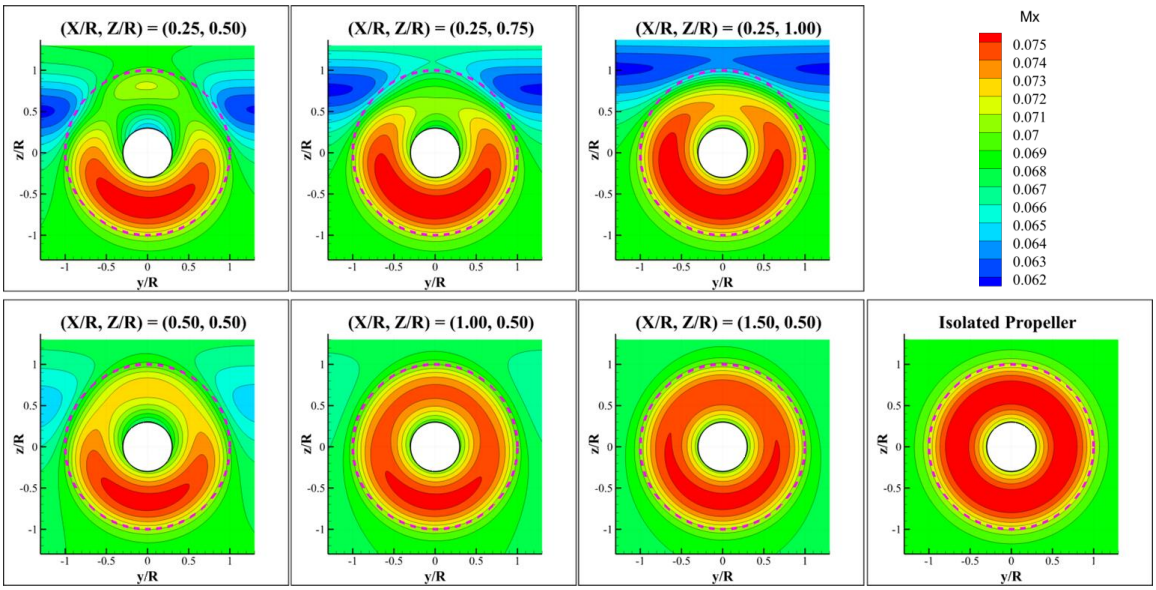

Figure 12. Contours of azimuthally averaged axial Mach number upstream of the propeller plane for all OF2 simulation conditions. Dashed circle denotes perimeter of propeller disk.

C_p distributions are not shown for the other conditions for the sake of brevity and due to negligible changes in measured pressures on the wing for changes in axial position. These negligible changes can be explained by the very little amount of propeller slipstream contraction that occurs over the range of tested axial wing positions. Overall, the predicted pressure trends agree well with the experimental measurements. Figures 13(a), 13(c), and 13(e) show both a gradual reduction in suction peak amplitude and stagnation amplitude on the side of the advancing propeller blade as the wing is moved further out of the propeller slipstream. A similar behavior is observed in Figs. 13(b), 13(d), and 13(f) on the side of the retreating propeller blade. This behavior is indicative of an increase in local dynamic pressure experienced by the immersion of the wing in the propeller slipstream.

Figure 14 shows the change in wing C_p on the advancing blade side for changes in both wing and propeller angles of attack for a wing leading edge position of $\left(\frac{\Delta X}{R}, \frac{\Delta Z}{R}\right) = (0.25, 0.50)$. The data show a clear expected increase in the suction peak amplitude with an increase in α_W. Furthermore, there is little to no change in the wing C_p distribution between conditions of $(\alpha_P, \alpha_W) = (0°, +5°)$ and $(\alpha_P, \alpha_W) = (+5°, +5°)$. Very similar behavior was observed for the other tested vertical wing locations. This indicates that the mean pressures on the wing immersed in the propeller slipstream are most sensitive to the wing angle of attack, and have little dependence on the propeller angle of attack.

3. Wing Unsteady Pressures

As mentioned previously, the unsteady pressure sleeve was positioned at two wing locations during this test: at a lateral location of $0.866R$ from the propeller centerline, and along the propeller centerline itself. These positions are intended to respectively measure the unsteady pressures on the wing that are caused by tip vortex impingement and inboard wake impingement. Figure 15 provides unsteady pressure data in the form of both root-mean-square pressure coefficients $\left(C'_{p,RMS}\right)$ and revolution-averaged perturbation pressure coefficient time histories at prescribed wing locations. Figures 15(a) and 15(d) provide illustrations of these measurement locations. Figure 15(b) shows a steep roll-off in $C'_{p,RMS}$ with increasing chordwise location, with the highest amplitude occurring at $x/c_s = 0.02$ on both pressure and suction sides. The per-revolution averaged pressure time histories at $x/c_s = 0.02$ on both the suction and pressure sides of the sleeve in Fig. 15(c) show a prominent negative pressure impulse at the pressure side sensor, which is likely due to the tip vortex impingement. Furthermore, Fig. 15(e) shows the variation of $C'_{p,RMS}$ at the leading edge sensors for different $\Delta Z/R$. The data show a steady rise in $C'_{p,RMS}$ for the suction side sensor up until $\Delta Z/R = 0.875$, after which it rapidly decreases. Note that this peak value of $C'_{p,RMS}$ is nearly twice the amplitude of that measured in the tip vortex trajectory (Fig. 15(b)). It is also worth noting that this

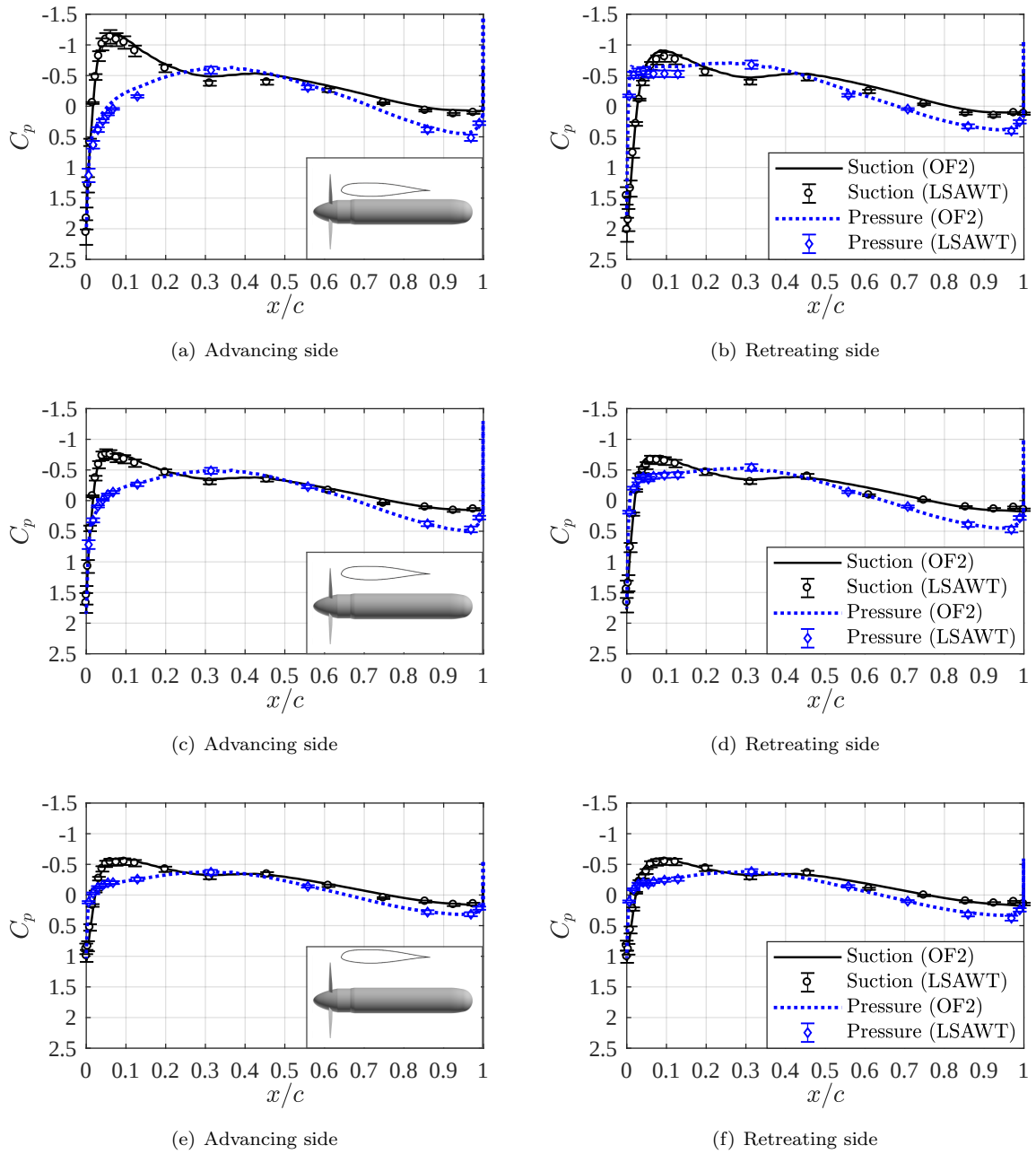

(a) Advancing side

(b) Retreating side

(c) Advancing side

(d) Retreating side

(e) Advancing side

(f) Retreating side

Figure 13. Wing steady pressure (C_p) comparisons between LSAWT measurements and OF2 predictions. Images (a), (b): $\left(\frac{\Delta X}{R}, \frac{\Delta Z}{R}\right) = (0.25, 0.50)$, (c), (d): $\left(\frac{\Delta X}{R}, \frac{\Delta Z}{R}\right) = (0.25, 0.75)$, (e), (f): $\left(\frac{\Delta X}{R}, \frac{\Delta Z}{R}\right) = (0.25, 1.00)$.

location $\Delta Z/R = 0.875$ approximately coincides with typical propeller blade spanwise regions of maximum loading. Finally, Fig. 15(f) provides the per-revolution averaged time histories of the suction and pressure side leading edge sensors at this inboard measurement location. The pressure oscillations are considerably broader in nature and are more qualitatively representative of the periodic wake being shed by the propeller blade passage events, rather than tip vortex impingement.

Figure 16 provides comparisons of wing RMS pressures between LSAWT measurements and OF2 predictions along both inboard wake and tip vortex trajectory measurement regions for respective vertical and axial wing placement variations. If attention is focused on Figs. 16(a), 16(c), and 16(e), overall agreement in trends can be seen between LSAWT measurements and OF2 predictions. The largest discrepancies for these comparisons lie in Fig. 16(a), where a "swap" in behavior between the OF2 and LSAWT data can be

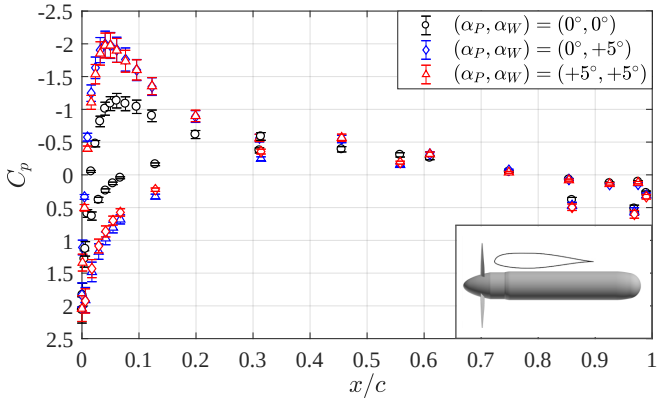

Figure 14. Wing C_p measurements on advancing blade side of propeller for changes in wing and propeller angles of attack for $\left(\frac{\Delta X}{R}, \frac{\Delta Z}{R}\right) = (0.25, 0.50)$.

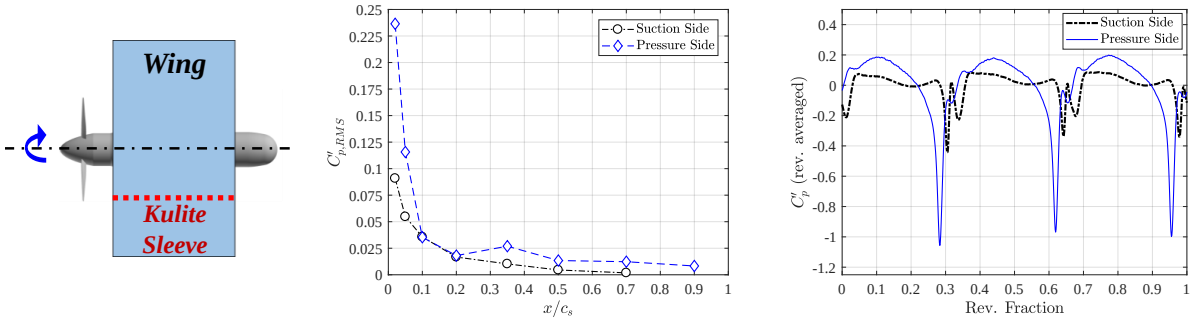

(a) Tip Vortex Trajectory (b) (c) $\left(\frac{\Delta X}{R}, \frac{\Delta Z}{R}\right) = (0.50, 0.50)$

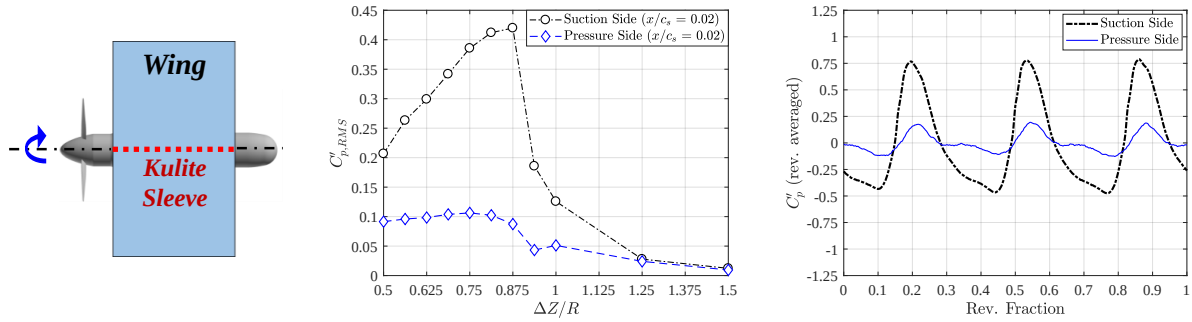

(d) Inboard Wake (e) (f) $\left(\frac{\Delta X}{R}, \frac{\Delta Z}{R}\right) = (0.25, 0.875)$

Figure 15. Periodically-averaged (b), (e) RMS pressure fluctuations and (c), (f) pressure time histories at wing leading edge ($x/c_s = 0.02$). Note that all data are averaged on a propeller per-revolution basis. Note: Images (a)-(c) represent wing position condition $\left(\frac{\Delta X}{R}, \frac{\Delta Z}{R}\right) = (0.50, 0.50)$, while images (d)-(f) represent a constant $\frac{\Delta X}{R} = 0.25$.

observed for the suction and pressure side leading edge regions. This is believed to be due to slight differences in the wing inclination angle relative to the propeller slipstream, either geometric or effective (such as that induced by flow turning in the LSAWT open jet test section). Figure 16(c) shows a considerable increase in suction side RMS pressures, with the highest amplitudes occurring near $x/c_{(s)} = 0.02$. Note that $x/c_{(s)}$ represents a common reference to both the simulated wing dimension of chord c and the experimentally measured transducer sleeve chord length c_s. While there is still a discrepancy in the peak $C'_{p,RMS}$ values between the two data sets, the trends agree very well. Furthermore, Fig. 16(e) shows an increase in pressure side RMS pressures in the range of $0.1 \leq x/c_{(s)} \leq 0.35$ between both data sets, with a sharp roll-off in RMS pressures on the suction side. This trend is caused by the suction side of the wing no longer being within

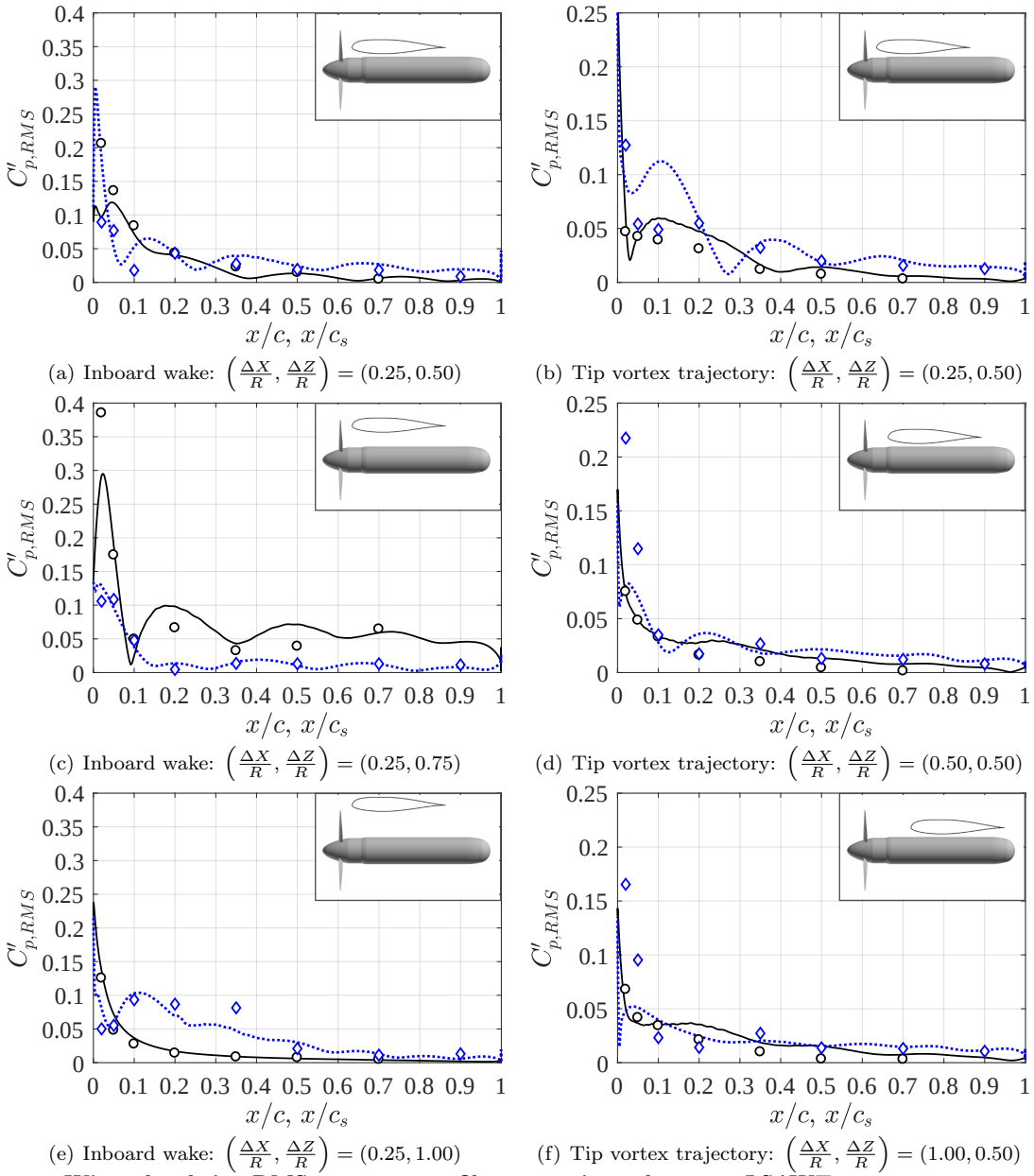

(a) Inboard wake: $\left(\frac{\Delta X}{R}, \frac{\Delta Z}{R}\right) = (0.25, 0.50)$

(b) Tip vortex trajectory: $\left(\frac{\Delta X}{R}, \frac{\Delta Z}{R}\right) = (0.25, 0.50)$

(c) Inboard wake: $\left(\frac{\Delta X}{R}, \frac{\Delta Z}{R}\right) = (0.25, 0.75)$

(d) Tip vortex trajectory: $\left(\frac{\Delta X}{R}, \frac{\Delta Z}{R}\right) = (0.50, 0.50)$

(e) Inboard wake: $\left(\frac{\Delta X}{R}, \frac{\Delta Z}{R}\right) = (0.25, 1.00)$

(f) Tip vortex trajectory: $\left(\frac{\Delta X}{R}, \frac{\Delta Z}{R}\right) = (1.00, 0.50)$

Figure 16. Wing chordwise RMS pressure profile comparisons between LSAWT measurements and OF2 predictions along inboard wake and tip vortex trajectory survey regions. Note: (−) OF2 suction side, (···) OF2 pressure side, (◯) LSAWT suction side probes, (◇) LSAWT pressure side probes.

the propeller slipstream at $\Delta X/R = 1.00$, while the pressure side is still at least partially immersed. Finally, Figs. 16(b), 16(d), and 16(f) show reasonable agreement between data sets in terms of RMS pressure roll-off in the chordwise direction, however with considerable discrepancies near the leading edge region. While the exact cause for these discrepancies is currently unknown, it is believed to be due to the OF2 simulations potentially underresolving the propeller tip vortex core structure.

B. Acoustic Measurements

1. Setup and Installation Effects

One challenge with the current test configuration is acoustic contamination from the brushless motor and electronic speed controller system. Because the propeller and motor have a 1:1 connection path (i.e., no gear reduction mechanism), the fundamental rotational frequencies of the two are the same. Therefore, the motor exhibits deterministic acoustic content that can be similar to that of the propeller. Figure 17

provides in-plane ($\theta = 93°$) spectra as well as tonal directivity comparisons for isolated propeller and motor only configurations. Figure 17(a) provides the narrowband acoustic spectra of the two cases, as well as

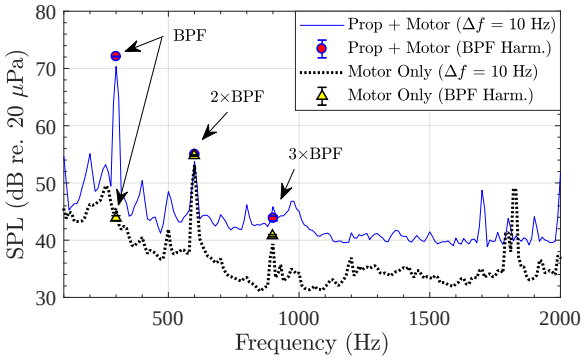

(a) Narrowband spectra ($\theta = 93°$)

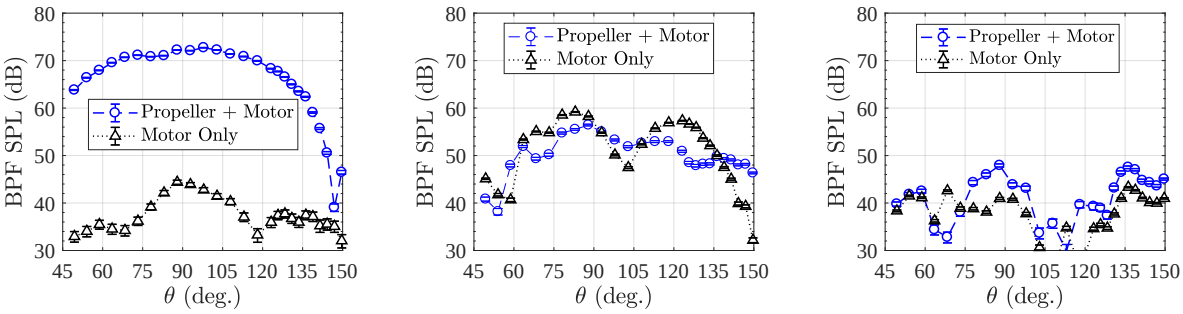

(b) BPF directivity (c) 2×BPF directivity (d) 3×BPF directivity

Figure 17. Propeller/motor signal-to-noise considerations at propeller BPF harmonics. Note that all cases shown are with freestream flow at $M_\infty = 0.068$.

the extracted BPF, 2×BPF, and 3×BPF tonal amplitudes of 300, 600, and 900 Hz, respectively. These correspond to a mechanical rotation rate of $\Omega_m = 6000$ RPM. It can be seen that the motor only case exhibits 2× and 3×BPF amplitudes that are either at or within 3 dB of the propeller operation case. The measured directivities of these tones are shown in Figs. 17(b), 17(c), and 17(d) for the two cases. These results show that while the propeller BPF levels are well above those for the motor only case, the other two harmonics are either comparable or sometimes below those of the motor itself. Therefore, the remainder of the acoustic results shown in this paper (both measurement and prediction) will focus on the propeller BPF. While this is an unfortunate limitation of the current dataset, predictions of the higher BPF harmonic levels were all found to be well below (at least 5 dB) that of the BPF itself, for all simulated propeller-wing configurations.

As was discussed in Section II.A, there is a considerable amount of testing hardware between the source regions of interest (propeller and wing) and the LSAWT microphone array. While the majority of the traverse rail surfaces are treated with acoustic foam panels, the panels are relatively thin with a thickness of approximately 0.1 m (4"). As a result, their absorption capabilities for frequencies below 1 kHz are unknown. Therefore, it is important to assess the acoustic behavior of the propeller system with and without the traverse and wing hardware present in the test cell. Figure 18 shows a comparison of propeller BPF acoustic directivity measurements for the isolated propeller with no traverse or wing hardware present, the isolated propeller with the traverse and wing hardware in a stowed position (wing upstream and below

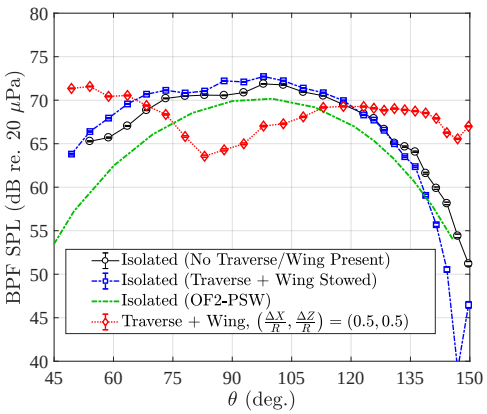

Figure 18. Acoustic BPF directivity of propeller and select propeller-wing configurations.

open jet core flow), an OF2-PSW prediction of the isolated propeller (no wing present), and a representative propeller-wing interaction condition $\left(\frac{\Delta X}{R}, \frac{\Delta Z}{R}\right) = (0.50, 0.50)$. It is worth noting that although there are some differences between the two isolated propeller test configurations, they are seen to be minor and exhibit very similar overall directivity shapes. Furthermore, the isolated propeller OF2-PSW prediction is seen to agree well with the BPF directivity trends of the two LSAWT isolated propeller measurements, however, with an underprediction in overall levels. This underprediction is due to the underprediction in thrust and torque generated by the propeller, discussed previously in Section III.A.1. The propeller-wing interaction case, however, displays a dramatically different behavior. The causes of this change in directivity are discussed in the following sections.

2. *Propeller-Wing BPF Acoustic Directivities*

Figure 19 shows a series of BPF directivity comparisons between different vertical wing positions and the isolated propeller BPF directivity (traverse and wing stowed condition), for a constant axial wing placement of $\Delta X/R = 0.25$. The results show a considerable variation in the directivity behavior for conditions in

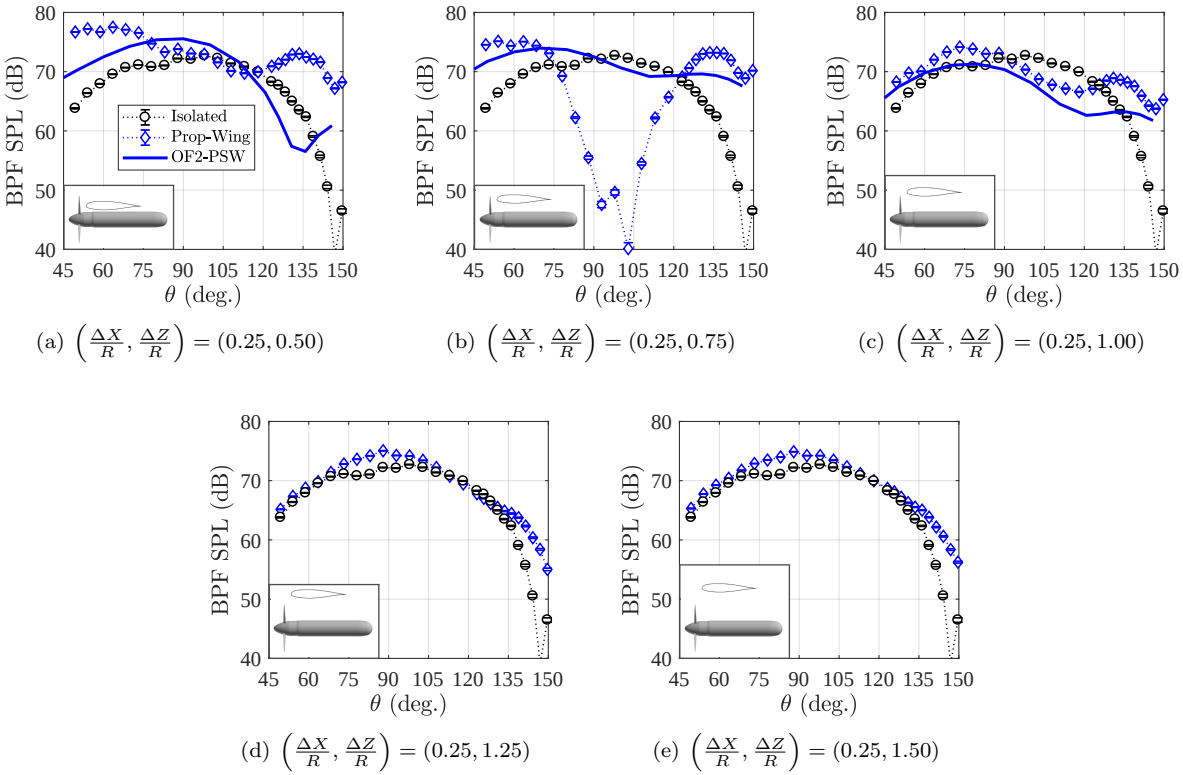

Figure 19. Measured propeller BPF acoustic directivity for different vertical wing positions at a constant axial location of $\Delta X/R = 0.25$. Note: ···○··· isolated propeller with stowed traverse system, ···◇··· propeller-wing condition.

which the wing is located at least partially within the propeller slip stream ($\Delta Z/R \leq 1.00$, Figs. 19(a) - 19(c)). Interestingly, Fig. 19(b) shows a very prominent null region, evident just aft of the propeller plane. Furthermore, Figs. 19(d) and 19(e) show the BPF directivities for the two cases in which the wing is outside of the propeller slipstream. It is interesting to note how the directivities for these two conditions are nearly identical to each other and also how they more closely resemble that of the isolated propeller case, however, with slightly elevated levels across observer ranges of $75° \leq \theta \leq 100°$ and $135° \leq \theta \leq 150°$. The data in Figs. 9(a) and 15(e) for these wing positions reveal respective propeller C_T very similar to the isolated propeller data, as well as very low $C'_{p,RMS}$ fluctuations at the wing leading edge. These measurements corroborate the notion that these propeller-wing conditions are approximately representative of the superposition of the cases of an isolated propeller and wing in axial forward flight. It is believed that these conditions will be helpful in determining the relative roles of reflections and scattering in the LSAWT

test section.

Figures 19(a) - 19(c) also have the accompanying OF2-PSW BPF acoustic directivity trends included for the appropriate wing positions. The first two predictions are seen to compare poorly with the LSAWT measurements; however, Fig. 19(b) shows reasonable agreement across observer angles in the range of $45° \leq \theta \leq 75°$ and $120° \leq \theta \leq 150°$. The null behavior evident in the LSAWT measurements for this condition is completely absent in the OF2-PSW prediction. The comparison shown in Fig. 19(c) is in contrast to the first two predictions in that it shows good agreement in BPF directivity trends between the data sets across the entire range of measured elevation angles.

Figure 20 shows the experimentally measured BPF directivities for the full range of tested axial positions for a constant vertical wing position of $\Delta Z/R = 0.5$, as well as OF2-PSW predictions for the cases of $\Delta X/R = 0.50$, 1.00, and 1.50 in Figs. 20(a), 20(c), and 20(e). In general, the OF2-PSW predictions do

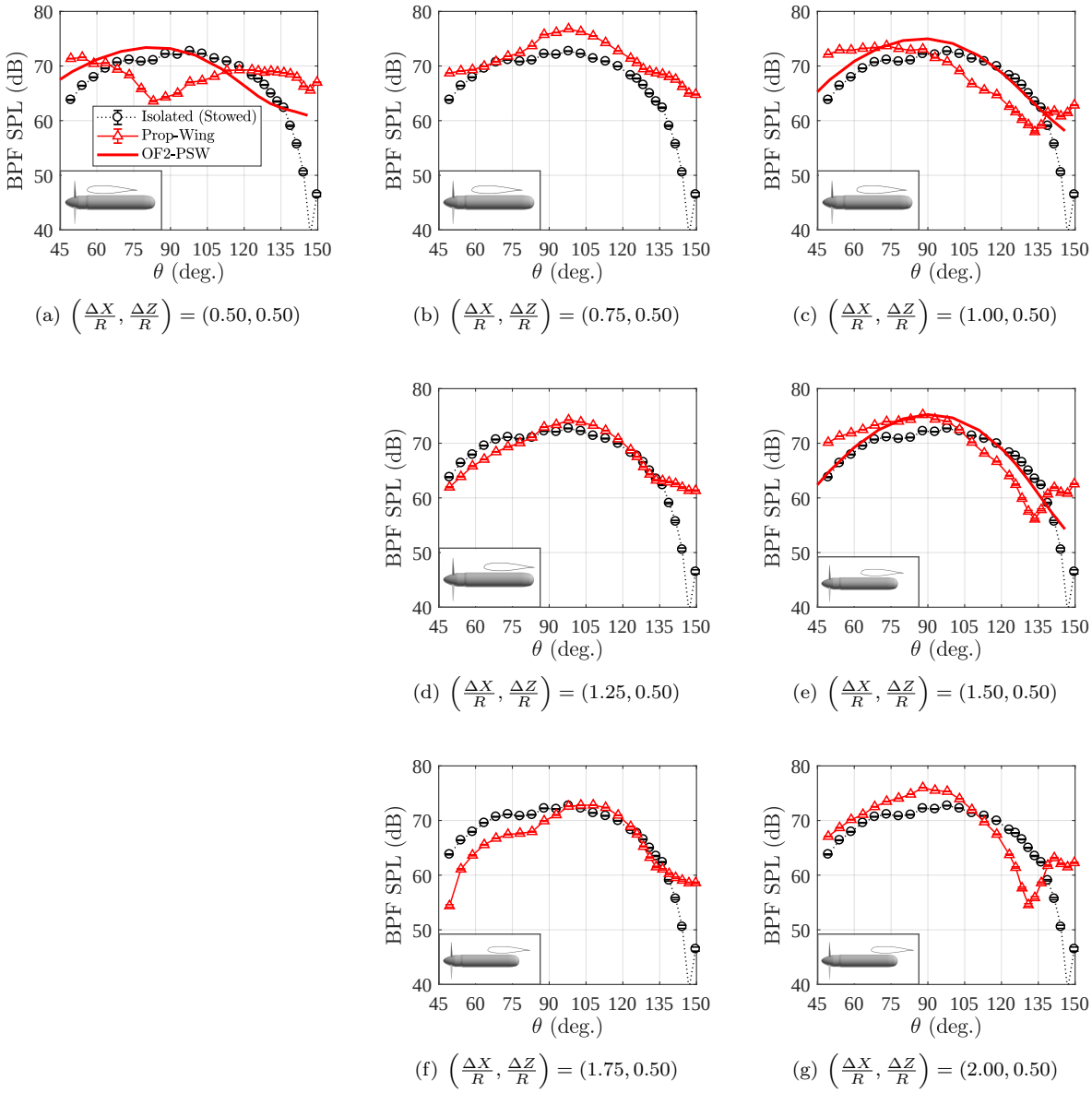

Figure 20. Measured propeller BPF acoustic directivity for different axial wing positions at a constant vertical location of $\Delta Z/R = 0.50$. Note: $\cdots\bigcirc\cdots$ isolated propeller with stowed traverse system, $-\triangle-$ propeller-wing condition.

not accurately capture the behaviors exhibited by their experimental counterparts; however, the prediction accuracy seems to improve as the wing is moved further downstream from the propeller disk. If attention

is focused on the experimental data in Fig. 20, it can be seen that with the exception of Fig. 20(a), the other figures follow an interesting alternating directivity trend with wing position. To better visualize this, these BPF directivity trends are reproduced in Fig. 21. As Fig. 21(a) shows, the cases of $\Delta X/R = 0.75$, 1.25, and 1.75 all have similar directivity shapes, with decreasing amplitudes as the wing is moved further downstream from the propeller disk. The case of $\left(\frac{\Delta X}{R}, \frac{\Delta Z}{R}\right) = (1.75, 0.50)$ is seen to be the quietest of these configurations, exhibiting BPF levels at or below those of the isolated propeller across the majority of the measured angles (see Fig. 20(f)). A different behavior is observed in Fig. 21(b), where acoustic levels are seen to decrease for $45° \leq \theta < 75°$ yet increase for $75° \leq \theta \leq 120°$ as the wing is moved further downstream. In general, this trend is indicative of a narrowing, or sharpening directivity trend, with peak levels occurring in the vicinity of the propeller plane ($\theta = 90°$).

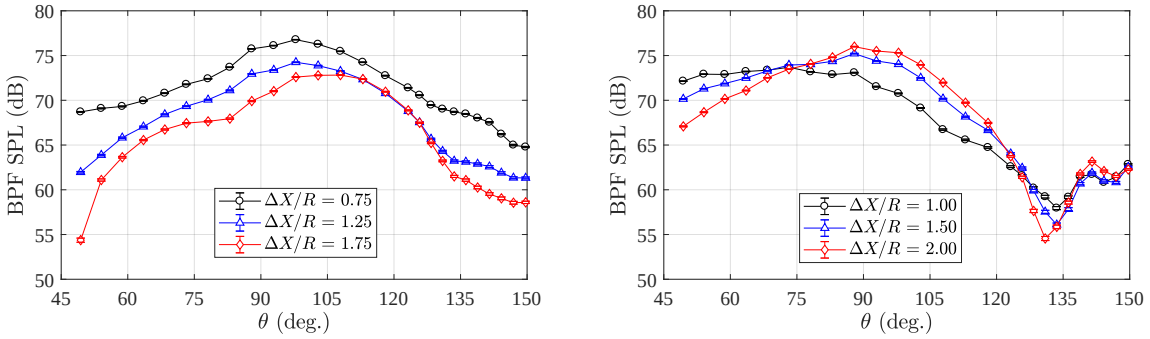

(a) (b)

Figure 21. Comparison of BPF directivities across different groupings of wing axial locations. All data shown are for $\Delta Z/R = 0.5$.

As mentioned previously, several propeller advance ratios were tested in addition to the primary one investigated. This was done in order to assess the sensitivity of the radiated acoustics to parameters like propeller disk loading and the resulting pressure loading on the wing. These were done for the wing positions of $\left(\frac{\Delta X}{R}, \frac{\Delta Z}{R}\right) = (0.50, 0.50)$ and $(0.25, 0.75)$. The first of these wing locations was selected for a broad sweep of propeller advance ratio (J), keeping M_{tip} constant, while varying M_∞. The second of these wing locations was selected for a much finer variation of J by varying M_{tip}. Figure 22 provides the BPF directivities for these two data sets. As Fig. 22(a) shows, the BPF directivity of the propeller-wing system varies widely

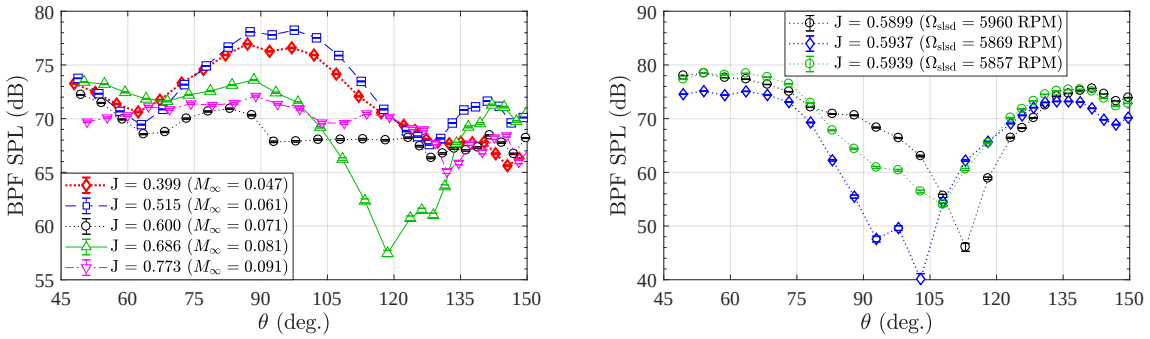

(a) Constant $M_{\text{tip}} = 0.371$, $\left(\frac{\Delta X}{R}, \frac{\Delta Z}{R}\right) = (0.50, 0.50)$ (b) Constant $M_\infty = 0.068$, $\left(\frac{\Delta X}{R}, \frac{\Delta Z}{R}\right) = (0.25, 0.75)$

Figure 22. Impact of advance ratio variations on BPF directivity for select propeller-wing configurations.

with advance ratio via variation in freestream Mach number. The results of Fig. 22(b) show comparable, if not more widely varying BPF levels, for small changes in advance ratio via changes in propeller tip Mach number. Note that this figure denotes the changes in tip speed by sea-level standard-day values of RPM (Ω_{slsd}). These results show up to 20 dB variation at certain observer locations for modest changes in tip Mach number. Concurrently, there is little variation seen in the directivity levels for observer angles in the ranges of $45° \leq \theta \leq 75°$ and $130° \leq \theta \leq 150°$. While the exact causes of these variations are unknown, they are likely the result of complex phase relationships between loading noise emanated from both the propeller and wing geometries, as well as interaction of these incident acoustic pressure waves with reflective surfaces in the facility. These possible mechanisms are investigated in more detail in the following sections.

3. *Predicted Surface Acoustic Contributions*

As was discussed in Section II.B.1, acoustic predictions are performed using the impermeable surface data of the different geometric components in the OF2 simulation. An illustration of the different surface contributions to the total propeller BPF acoustic directivity is provided in Fig. 23. As Fig. 23(b) shows, the

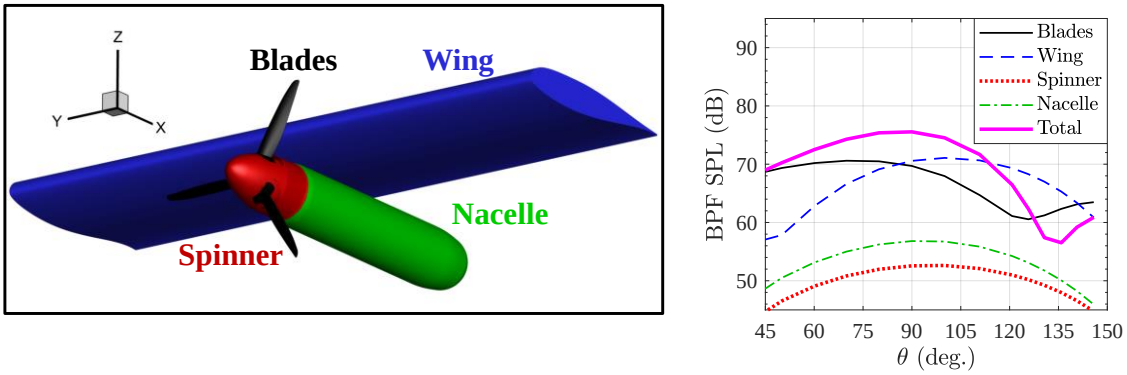

(a) Impermeable surfaces used in PSW predictions

(b) Surface contributions

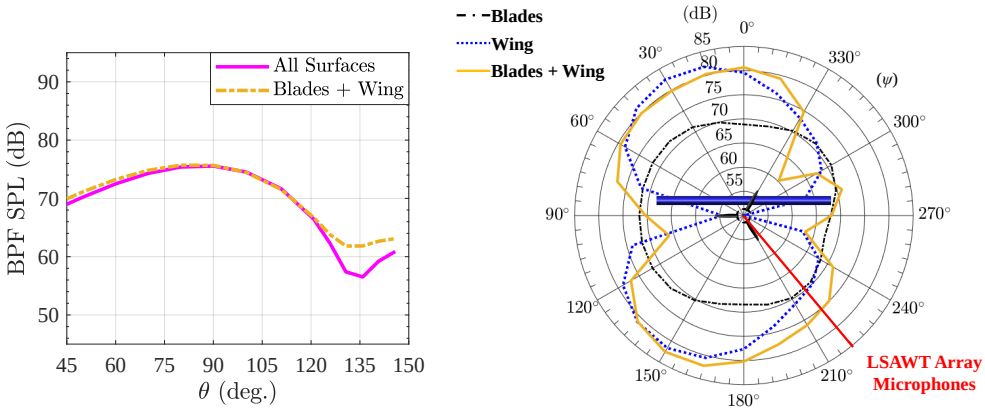

(c) All surfaces vs. blades + wing

(d) In-plane ($\theta = 90°$) azimuthal directivity

Figure 23. Impermeable surface contributions to radiated noise at propeller BPF for $\left(\frac{\Delta X}{R}, \frac{\Delta Z}{R}\right) = (0.25, 0.50)$.

majority of noise is generated by the propeller and wing surfaces. This is important because it identifies that the wing both affects the propeller inflow (and thus radiated noise), and acts as a separate loading noise source. This type of behavior was identified in the rotor-airframe interaction study of Reference 12. Another important observation is the acoustic content of the spinner and nacelle surfaces. While the acoustic levels generated by these surfaces are low relative to the propeller blades and wing surfaces, Fig. 23(c) illustrates the effect of removing these surfaces from the total radiated acoustic directivity. While the acoustic levels for the majority of observer angles are seen to be well defined by the propeller blades and wing surfaces, the acoustic levels for the aft range of observer angles are seen to differ by up to 6 dB by not including the spinner and nacelle surfaces. Because of this, all surfaces were used to generate the results presented in the previous section. Figure 23(d) presents the azimuthal (ψ) directivity in the plane of the propeller. The results reveal a directivity of the propeller blades that resembles a distorted monopole, while that for the wing resembles a skewed dipole that is symmetric about the horizontal plane defined by $\psi = 90°, 270°$. This symmetry is expected to degrade with changes in wing angle of attack. These results, along with those in Fig. 23(b), show that the wing can play a very important and sometimes dominant noise generation role under the flight path, particularly between $120° \leq \phi \leq 180°$. Note that the following results will focus on the acoustics associated with the propeller and wing surfaces because they are the major contributors.

Figure 24 provides the predicted contributions of the propeller blades and wing surfaces for the vertical sweep of simulated wing locations. Figure 24(a) shows a considerable change in the propeller directivity between $\Delta Z/R = 0.50$ to 0.75, with only a modest change from $\Delta Z/R = 0.75$ to 1.00. Figure 24(b) shows an increase in BPF SPL radiated by the wing across the entire range of predicted directivity angles anywhere

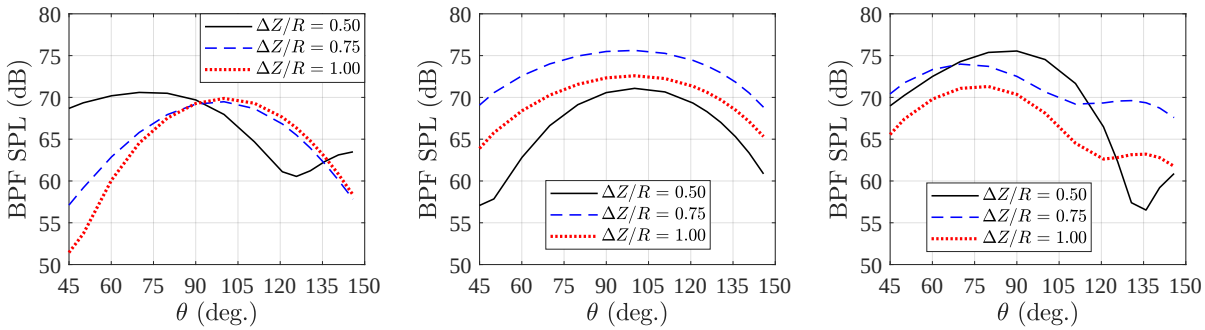

(a) Propeller blades contribution (b) Wing surface contributions (c) All surfaces

Figure 24. Propeller blades and wing surface impermeable surface contributions to BPF acoustic directivities for wing vertical sweep locations. All predictions shown are for $\Delta X/R = 0.25$.

between 5 dB and 12 dB from $\Delta Z/R = 0.50$ to 0.75. These levels are then slightly reduced for $\Delta Z/R = 1.00$. The high BPF levels radiated by the wing at $\Delta Z/R = 0.75$ are believed to be associated with the increase in wing leading edge RMS pressure fluctuations shown previously in Figs. 15(e) and 16(c). Finally, Fig. 24(c) provides the BPF directivities for these wing locations that are comprised of all computational surfaces. This figure illustrates the complexity of the acoustic field, since the resultant acoustic directivities are not necessarily intuitive based on the individual surface contributions. This is because of the complex phase relationships between the different sources that have functional dependence on directivity angle.

Figure 25 provides the predicted contributions from the propeller blades and wing surfaces for the axial sweep of simulated wing locations. Similar to the vertical sweep results, Fig. 25(a) shows a dramatic shift in

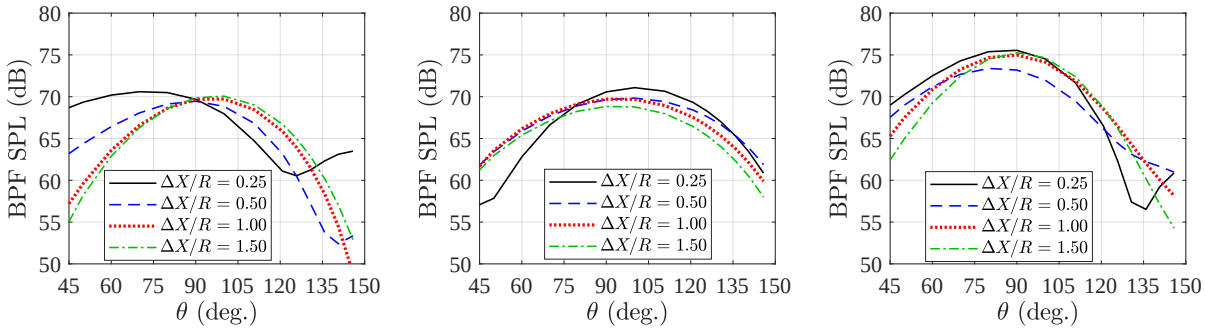

(a) Propeller blades contribution (b) Wing surface contributions (c) All surfaces

Figure 25. Propeller blades and wing surface impermeable surface contributions to BPF acoustic directivities for wing axial sweep locations. All predictions shown are for $\Delta Z/R = 0.50$.

propeller-radiated BPF directivity between $\Delta X/R = 0.25$ to 0.50. Figure 25(b) shows similar results for the wing contribution, where the wing exhibits very similar radiated noise for the cases of $\Delta X/R = 0.50$, 1.00, and 1.50. This dramatic initial change in directivity for the propeller blades and wing is indicative of a near- to far-wake interaction phenomenon. The gradual decrease in radiated noise from the wing between $\Delta X/R = 0.50$ and 1.50 implies a persistent pressure loading on the wing from the propeller wake that is gradually weakened as it moves further downstream. Figure 25(c) compares the directivities of the simulated axial wing locations using all computational surfaces. The trends in this figure reveal a very similar directivity sharpening behavior as those shown in the experimental data of Fig. 21(b).

4. Acoustic Scattering and Reflections

The comparisons between CFD-based acoustic predictions and experimental measurements in Section III.B.2 were found to contain discrepancies for some of the tested propeller-wing configurations. One of the likely explanations for this is acoustic scattering from the wing, traverse, MPTS, and other facility components such as the upstream inlet nozzle and downstream flow collector. A considerable challenge to modeling this

behavior lies in the fact that the wing itself is evidenced to be a very important noise radiator as well as a likely reflective source. As mentioned previously, the source region is modeled in the TD-FAST code as a simple monopole source positioned at the propeller hub. This obviously does not account for the directivity behavior of the propeller, nor does it account for the loading noise generated by the wing. However, usage of a simple, known source behavior is believed to provide useful intuition in assessing the potential impacts of the facility on the incident source noise. Since the loading noise on the wing cannot be currently modeled in the TD-FAST code, scattering predictions are performed at a common vertical position of $\Delta Z/R = 1.50$. These conditions should nearly eliminate the wing as a noise radiator at the characteristic propeller frequencies (BPF harmonics), while still modeling its effects as a reflective source.

The scattered pressure field is numerically represented by a shielding function γ, which is defined as

$$\gamma = 10 * \log_{10}\left(\frac{p^2_{\mathrm{RMS}}}{p^2_{\mathrm{RMS,inc.}}}\right), \tag{1}$$

where p_{RMS} is the measured acoustic pressure including the scattered field and $p_{\mathrm{RMS,inc.}}$ is the incident pressure field free of scattering effects. While such an expression cannot be directly applied to the measured data, a simplified version is defined based on the measured directivity of the propeller-wing (PW) configuration in question relative to the isolated propeller (P) as

$$\gamma_{\mathrm{meas.}} = \mathrm{SPL_{PW}} - \mathrm{SPL_{P}}. \tag{2}$$

It is important to note that Eq. 2 is only applicable to cases where the incident pressure field is dominated by the propeller source. The tested conditions that best fit this criteria are those for which the wing is at a vertical location of $\Delta Z/R = 1.50$. Figure 26 provides the computed shielding results at a subset of wing locations.

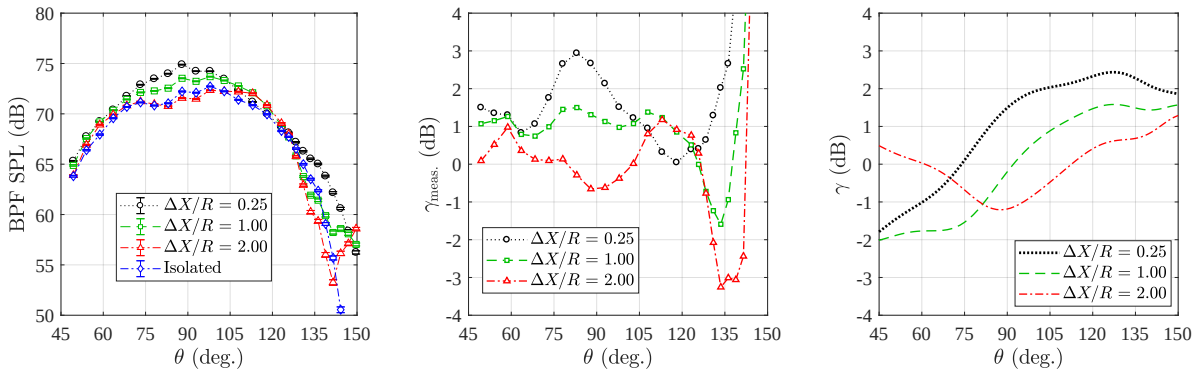

(a) BPF directivities (b) Measured shielding (c) Predicted shielding

Figure 26. Shielding function predictions and measurements for select propeller-wing interaction cases. $\Delta Z/R$ = 1.50 for all cases shown.

The results of Fig. 26(a) show that movement of the wing further downstream results in a decrease in levels in the regions $75° \leq \theta \leq 115°$ and $130° \leq \theta \leq 150°$, yielding a convergence of the BPF directivity to more closely resemble that of the isolated propeller. Figures 26(b) and 26(c) show the measured and predicted shielding functions computed using Eqs. 2 and 1, respectively. It is worth noting that the case of $\Delta X/R = 2.00$ contains similarities between measurement and prediction up to an observer angle of $\theta \approx 125°$. There is also a similar behavior between the data sets comprising a transition from positive γ (constructive interference) to negative γ (destructive interference) in the vicinity of the propeller plane, $\theta = 90°$, as the wing axial location moves further downstream. While the amplitudes of variation between the measured and predicted data sets are comparable to one another, there are considerable overall discrepancies in the shielding directivity trends, particularly at angles far downstream of the propeller plane.

There are several possible explanations for the discrepancies shown in the scattered acoustic field results. As shown in Fig. 8(b), the test section hardware immediately surrounding the propeller were included in the predictions. Other surfaces such as the inlet nozzle and flow collector (see Fig. 8(a)) were not included in these simulations. These may be very important scattering surfaces due to their very large surface

areas, particularly for measurements far upstream and downstream of the propeller plane. In addition, the current definition of the propeller source as a stationary monopole could be a considerable misrepresentation, particularly because the propeller is a rotating source. Finally, it is assumed that the wing does not behave as a loading noise source at the largest tested vertical separation distance of $\Delta Z/R = 1.50$. Due to the complex phase relationships between the propeller and wing surfaces documented in the previous section, even modest noise contributions from the wing can alter the shape of the measured BPF directivity.

A final factor that is considered here is the predicted relative contributions of the test section hardware and wing geometries as scattering surfaces. Figure 27 shows the predicted shielding function contributions of the sting plate, fairing, traverse rails, and wing geometries, as well as the total shielding function comprised of all of these components. The results are for those shown previously in Fig. 26(c) for $\Delta X/R = 2.00$. The results show that the sting plate and fairing surfaces contribute minimally to the scattered acoustic field. Furthermore, while the traverse rails do have a moderate contribution, the amplitudes of variation are within ±0.75 dB. The wing surface, however, exhibits a much larger variation, spanning from a -2 dB reduction at $\theta = 85°$ to a +1.5 dB increase at $\theta = 135°$. While these levels of variation are not overly large, it is important to recall the limitations of the current scattering prediction: the single source is a stationary monopole that does not accurately represent the rotational propeller noise sources, and the wing has a larger vertical spacing from the propeller than what might be practical for an actual vehicle. Therefore, it is likely that the relative magnitudes of scattering by the wing geometry could be larger for a more realistic inboard propeller-wing configuration.

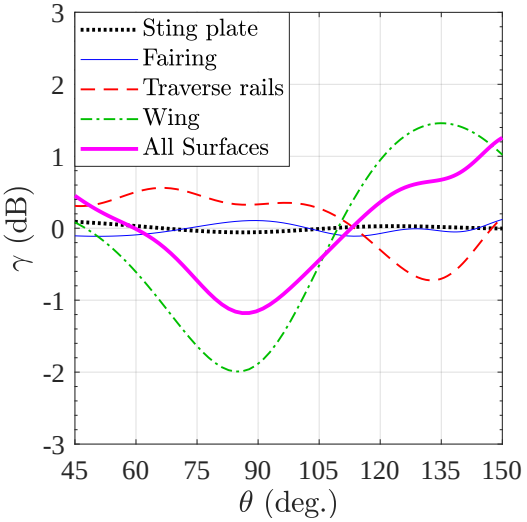

Figure 27. TD-FAST shielding function prediction contributions by individual test section components relative to the total test section hardware prediction. Cases shown are for $\Delta X/R = 2.00$.

IV. Conclusions and Future Work

This paper presents aerodynamic and acoustic results from an experimental testing and computational prediction campaign that investigated different inboard propeller-wing configurations. The primary parameters of interest were the wing leading edge location relative to both the propeller disk and hub, respectively.

Variations in propeller thrust measurements show good agreement with predictions for a survey of vertical wing positions, however, they also show discrepancies for axial wing locations downstream from the propeller disk. This is believed to be due to considerable differences in the interface region between motor and nacelle geometries between the experimental test setup and CFD computational domain. Such discrepancies are certainly possible because this interface region corresponds to the approximate location of the measurement face of the load cell. Visualization of predicted axial velocity contours at a plane upstream of the propeller reveal inflow distortion effects imposed by the wing potential field that are gradually reduced as the wing is traversed further away from the propeller disk (axially) and from the hub (vertically).

Chordwise steady pressure profiles on the wing surface revealed excellent agreement with predictions on both advancing and retreating blade sides. Appropriate shifts in trends were observed as the wing was vertically moved further from the propeller hub. Wing unsteady pressure measurements of the propeller inboard wake revealed peak RMS pressures at the wing leading edge location approximately coinciding with a region of expected maximum loading on the propeller blade. Tip vortex trajectory unsteady pressure measurements revealed impulsive behavior at the wing leading edge indicative of tip vortex impingement. These impulsive RMS pressures, however, were considerably lower in amplitude than the inboard wake measurements. Good agreement in inboard wake RMS pressure trends was found between experiment and predictions for vertical wing movements, while discrepancies were found in the leading edge region of the tip vortex trajectory measurements for axial wing movements. Possible explanations for these discrepancies include slight misalignment of the wing effective angle of inclination relative to the propeller (due to the experimental open jet test section), as well as the CFD simulation not fully resolving the shape and intensity

of the propeller tip vortices.

Acoustic comparisons between experiments and predictions were limited to the fundamental propeller BPF due to motor noise contamination of the higher harmonics. Experimental results reveal dramatic variations in BPF directivity as a function of wing positions, both vertically and axially. The appearance of directivity nulls for certain wing positions is indicative of complex phase relationships between both propeller and wing noise sources as well as potential scattering and reflection effects within the test facility. These types of pressure nulls were not captured by CFD-based acoustic predictions, which are devoid of such scattering and reflection effects. Acoustic predictions reveal comparable contributions of both propeller and wing loading noise sources for all tested propeller-wing configurations, indicating that both wing potential field influences on the propeller inflow as well as propeller wake loading on the wing are important noise sources.

Initial attempts at predicting the scattered acoustic field were done by simulating a stationary point monopole source at the propeller hub location amongst simplified geometric surface representations of the test section hardware. Only a small subset of wing positions were considered because only conditions in which the wing is not expected to be a loading noise radiator are currently applicable. While initial scattering predictions do show BPF amplitude variations that are similar to those experimentally observed, the directivity trends do not agree very well. This is believed to be due to inappropriate modeling of the source region (such as a stationary monopole in place of rotating propeller blades) and the lack of inclusion of wind tunnel test section components of large surface area that are not acoustically treated. Finally, isolation of the traverse hardware and wing surfaces as scattering surfaces for a common wing position revealed the wing to be the most prominent scattering source. This implies that the wing surface on an actual UAM vehicle configuration could play a large scattering role.

Future work will include improvements to the MPTS to allow for more reliable acoustic interrogation of higher frequency propeller harmonics, with an emphasis on the reduction of motor noise. Analysis and interrogation of multipropeller and multipropeller-wing measurements will also be conducted in order to assess the impact of wing loading noise on phase-synchronized propeller systems. Finally, improvements to the acoustic scattering model will be implemented, including increased complexity of the source models used and inclusion of more of the wind tunnel test section hardware into the computations.

Acknowledgments

The authors would like to acknowledge Mr. John Swartzbaugh, Stanley Mason, Jeff Collins, Bryan Lamb, and Mick Hodgins of the Low Speed Aeroacoustic Wind Tunnel (LSAWT) at the NASA Langley Research Center for their tireless efforts involving test setup, facility operations, and data acquisition. The authors would also like to acknowledge Joseph Derlaga of the NASA Langley Computational Aerosciences Branch and Joshua Blake of the NASA Langley Aeroacoustics Branch for their assistance with CFD grid generation. Funding for this work is being provided by the NASA Transformative Tools and Technologies (TTT) project, which is part of the NASA Transformative Aeronautics Concepts Program (TACP).

References

[1]Farassat, F., "Linear Acoustic Formulas for Calculation of Rotating Blade Noise," *AIAA Journal*, Vol. 19, No. 9, Sep 1981, pp. 1122–1130.

[2]Brentner, K. and Farassat, F., "Modeling aerodynamically generated sound of helicopter rotors," *Progress in Aerospace Sciences*, Vol. 39, April 2003, pp. 83–120.

[3]Zawodny, N. S. and Haskin, H. H., "Small Propeller and Rotor Testing Capabilities of the NASA Langley Low Speed Aeroacoustic Wind Tunnel," *23rd AIAA/CEAS Aeroacoustics Conference*, Denver, CO, AIAA Paper 2017-3709, June 2017.

[4]Zawodny, N. S., Haskin, H., and Nark, D. M., "Aerodynamic Performance and Acoustic Measurements of a High-Lift Propeller in an Isolated Configuration," *2018 AIAA/CEAS Aeroacoustics Conference*, Atlanta, GA, AIAA Paper 2018-3448, June 2018.

[5]Hicks, R. M. and Schairer, E. T., *Effects of Upper Surface Modification on the Aerodynamic Characteristics of the NACA* $63_2 - 215$ *Airfoil Section*, Moffett Field, CA, NASA TM 78503, 1979.

[6]Hutcheson, F. V., Stead, D. J., and Plassman, G. E., "Experimental Study of Wake / Flap Interaction Noise and the Reduction of Flap Side Edge Noise," *22nd AIAA/CEAS Aeroacoustics Conference*, Lyon, France, AIAA Paper 2016-2955, May 2016.

[7]Sinnige, T., de Vries, R., Corte, B. D., Avallone, F., Ragni, D., Eitelberg, G., and Veldhuis, L. L. M., "Unsteady Pylon Loading Caused by Propeller-Slipstream Impingement for Tip-Mounted Propellers," *Journal of Aircraft*, Vol. 55, No. 4, 2018, pp. 1605–1618.

[8]Zawodny, N. S., Boyd Jr., D. D., and Burley, C. L., "Acoustic Characterization and Prediction of Representative , Small-Scale Rotary-Wing Unmanned Aircraft System Components," *AHS International 72nd Annual Forum*, American Helicopter Society, West Palm Beach, FL, 2016.

[9]Nichols, R. H. and Buning, P. G., *User's Manual for OVERFLOW 2.2*, NASA Langley Research Center, Available at http://overflow.larc.nasa.gov/home/users-manual-for-overflow-2-2/.

[10]Chan, W. M., Gomez III, R. J., Rogers, S. E., and Buning, P. G., "Best Practices in Overset Grid Generation," *Proceedings of the 32nd AIAA Fluid Dynamics Conference*, AIAA Paper 2002-3191, June 2002.

[11]Hu, F. Q., Pizzo, M. E., and Nark, D. M., "On the Assessment of Acoustic Scattering and Shielding by Time Domain Boundary Integral Equation Solutions," *22nd AIAA/CEAS Aeroacoustics Conference*, Lyon, France, AIAA Paper 2016-2779, May 2016.

[12]Zawodny, N. S. and Boyd, D. D., "Investigation of Rotor-Airframe Interaction Noise Associated with Small-Scale Rotary-Wing Unmanned Aircraft Systems," *Journal of the American Helicopter Society*, Vol. 65, No. 1, 2020, pp. 1–17.